International Journal of Nanomedicine

Dovepress
open access to scientific and medical research

Open Access Full Text Article

ORIGINAL RESEARCH

RGD Peptide and PAD4 Inhibitor-Loaded Gold Nanorods for Chemo-Photothermal Combined Therapy to Inhibit Tumor Growth, Prevent Lung Metastasis and Improve Biosafety

Yu Lu[1,2]
Zidong Peng[1,2]
Di Zhu[1,2]
Yijiang Jia[1,2]
Ayijiang Taledaohan[1,2]
Yuanming Li[3]
Jiawang Liu[4]
Yanming Wang[5]
Yuji Wang[1,2]

[1]Department of Medicinal Chemistry, College of Pharmaceutical Sciences of Capital Medical University, Beijing, 100069, People's Republic of China; [2]Beijing Area Major Laboratory of Peptide and Small Molecular Drugs, Engineering Research Center of Endogenous Prophylactic of Ministry of Education of China, Beijing Laboratory of Biomedical Materials, Beijing Laboratory of Oral Health, Beijing, 100069, People's Republic of China; [3]Invasive Tumor Therapies Center, Beijing Hospital, National Center of Gerontology, Beijing, 100730, People's Republic of China; [4]Medicinal Chemistry Core, The University of Tennessee Health Science Center, 579 College of Pharmacy Building, Memphis, TN, 38163, USA; [5]School of Life Sciences, Henan University, Kaifeng, 475004, People's Republic of China

Correspondence: Yuji Wang
10 Xi Tou Tiao, You An Men, Beijing, 100069, People's Republic of China
Tel +86-10-8391-1530
Fax +86-10-8391-1533
Email wangyuji@ccmu.edu.cn

Purpose: A targeted drug delivery system that combines protein-arginine deiminase type-4 (PAD4) inhibitors YW3-56 (356) with PTT of NPs is constructed to both decrease the accumulation of gold in metabolic organs and reduce the dose of chemotherapeutic agents.

Patients and Methods: In vitro cytotoxicity test and in vivo S180 tumor-bearing mice model were used to compare antitumor activity of 356-modified gold nanospheres and nanorods. The A549 tumor-bearing mice model was also exploited in antitumor assessment. In addition, ICP-MS, blood cell analyzer and blood biochemistry analyzer are applied for assessing the biosafety of NPs.

Results: Both 356-modified gold nanospheres and nanorods showed antitumor activity. However, 356-loaded gold nanorods are found to have better tumor inhibitory activity than 356-loaded gold nanospheres in the presence of laser and without laser irradiation. Thus, 356-loaded gold nanorods are selected to be applied for chemo-photothermal combined therapy on in vivo. We find that combination therapy could inhibit tumor growth and reduce lung tumor metastasis and inflammatory infiltration compared with individual therapy. It triggers apoptosis in tumor tissue observed by TUNEL assay and TEM pictures.

Conclusion: Thus, an RGD targeting and PAD4 inhibitor-loaded system are established based on chemo-photothermal combined therapy. It could inhibit tumor growth, prevent lung metastasis and improve biosafety.

Keywords: gold nanospheres, gold nanorods, PAD4 inhibitor, chemo-photothermal combined therapy, biosafety

Introduction

Peptidyl arginine deiminase 4 (PAD4) is an important enzyme in the post-translational modification of histones.[1–3] It catalyzes the conversion of arginine from histone to citrulline (citrullination).[4,5] Since PAD4 is associated with many human diseases, such as cardiovascular diseases,[6] ischemia-reperfusion (I/R),[7,8] neutrophil extracellular traps (NETs),[9] rheumatoid arthritis (RA)[10] and various tumors,[9,11] it has attracted the attention of many scientists. A number of reversible and irreversible inhibitors have been synthesized to inhibit the activity of PAD4 and thus prevent the occurrence of various diseases.[12–14] YW3-56 (356) was one of the inhibitors that has been shown to be able to suppress the citrullination of histone 3 (H3cit) and thus inhibit sarcoma growth.[14] However, its rapid metabolism and the

Received: 8 May 2021
Accepted: 2 August 2021
Published: 16 August 2021

Graphical Abstract

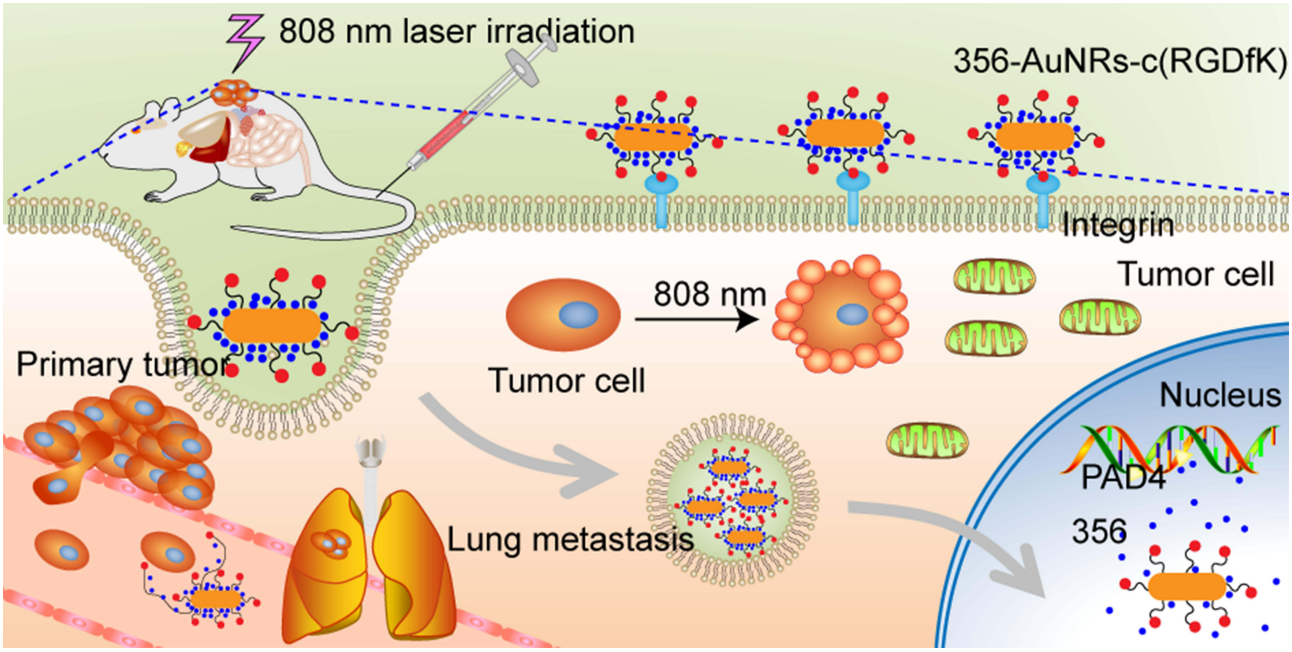

inherent biological toxicity of chemotherapeutic agents restrict the clinical development of 356.

In recent years, photothermal therapy (PTT) is attractive to more and more scientists.[15–18] It could target tumor sites accurately to reduce biological toxicity of systemic tissues, and laser irradiation from outside is a minimally invasive treatment.[19,20] Gold nanoparticles (NPs) have become an excellent photothermal transduction agent (PTA) because of their high photothermal conversion efficiency. Many types of NPs and their surface functionalized preparations have been used as PTA for the treatment of tumors,[21–27] including gold nanospheres (AuNPs)[28] and gold nanorods (AuNRs).[29–31] The ability of light-to-heat conversion could trigger tumor cell death through apoptosis or necrosis.[32,33] However, NPs may damage liver, kidney or other tissues because of the different accumulation level in organs and tumors. Many researchers have explored strategies to increase the tumor accumulation of PTAs, such as introducing targeting ligands to NPs[34] or changing the NPs size and shape.[35] RGD containing peptides are the ligand of integrin which is highly expressed on the surface of tumor cells.[36,37] Many drug-loaded systems or small molecules use RGD containing peptides as the target part of drug-loaded system to improve tumor targeting.[28,38–43] The peptide c(RGDfK) has been shown to interact with integrin receptor αVβ3 which is overexpressed on the surface of tumor cells.[44]

Our aim is to construct a targeted drug delivery system that combines PAD4 inhibitors with PTT of NPs. Synergistic effects of chemotherapy and photothermal therapy could improve the biosafety of drug-loaded systems. Surface-functionalized gold nanospheres (AuNPs-c-(RGDfK) and 356-AuNPs-c(RGDfK)) and gold nanorods (AuNRs-c(RGDfK) and 356-AuNRs-c(RGDfK)) were prepared. Their structures were confirmed by UV absorption spectra and transmission electron microscopy (TEM). The anti-tumor and anti-metastatic efficacies of 356-loaded NPs and 356 alone were compared by MTT and transwell assay with or without Matrigel in vitro. Confocal laser scanning microscopy (CLSM) and flow cytometry were used to determine the tumor permeability and uptake pathway of the drug-loaded system. In vivo, S180 sarcoma model was used to investigate the anti-tumor activity, and tumor sections were used to confirm tissue permeability and H3cit inhibition of 356-loaded NPs. 356-loaded gold nanorods were proved to have a better profile of tumor inhibitory activity and anti-metastatic activity compared with 356-loaded gold nanospheres. This may be related to the stronger cell and tissue permeability of 356-loaded gold nanorods. Thus, 356-loaded gold nanorods were

selected to be applied for chemo-photothermal combined therapy on A549 tumor-bearing mice in vivo. The gold content in different organs was determined by ICP-MS. In addition, blood routine index and blood biochemical index were measured by a blood cell analyzer and blood biochemistry analyzer, respectively. They were all used to assess the biological toxicity of mice after administration. Besides, apoptosis in tumor tissue was observed by TUNEL assay and TEM pictures.

Patients and Methods

Materials

Please refer to the supporting information for the materials and reagents used. Methods are recorded in the supporting information as follow: synthesis of AuNPs and AuNRs, synthesis of YW3-56, UV-Vis absorption spectra, transmission electron microscopy (TEM), Zeta potential, in vitro growth inhibitory effect of NPs, transwell assay with or without Matrigel, cellular uptake of NPs, uptake pathway determination, immunofluorescence and immunohistochemistry, in vivo biosafety of chemo-photothermal combined therapy, cell apoptosis of tumor tissues in vivo.

Statistical Analysis

All data were expressed as mean ± SD and analyzed by one-way ANOVA using Prism 7.0 software. All values were obtained from at least three independent experiments. $p < 0.05$ was considered to be statistically significant and $p < 0.01$ was considered to be extreme significance.

Synthesis

For the synthesis and identifications of YW3-56 and gold nanoparticles, please refer to supporting information 2.2 section.

Synthesis of AuNPs-c(RGDfK) and AuNRs-c(RGDfK)

Citrate-stabilized gold nanoparticles (AuNPs) are commonly synthesized by reducing tetrachloroauric acid with trisodium citrate.[39] 0.5 mg HS-PEG-COOH (3.4 kDa) was added into 5 mL aqueous AuNPs (0.1 mg Au/mL) overnight. The AuNPs were centrifuged (11,000 rpm, 10 min) and washed with deionized water to remove the excess free PEG and the AuNP pellet was redispersed in 5 mL deionized water. No aggregation was observed. c(RGDfK) peptide was conjugated onto the carboxyl terminal of AuNPs-PEG-COOH via EDC/NHS coupling reactions. First, EDC·HCl (4.98×10^{-2} mmol) and NHS (4.98×10^{-2} mmol) were individually dissolved in 500 μL PBS buffer (pH=7.4), added to 1 mL of a AuNPs-PEG-COOH solution (0.5 mg Au/mL), and allowed to react 2 h in the dark at room temperature. The reaction solution was centrifuged (11,000 rpm, 10 min) and washed with PBS buffer to remove the excess free EDC/NHS and the AuNP pellet was redispersed in 1 mL PBS buffer. Subsequently, 1 mL c(RGDfK) peptide (4.99×10^{-3} mmol) was added to the reaction mixture, followed by stirring for 6 h in the dark at room temperature. The final product was purified by centrifugation (11,000 rpm for 10 min at 4 °C), redispersed in 1 mL deionized water, and stored at 4 °C in the dark. AuNRs-c(RGDfK) was synthesized following a similar procedure as AuNPs-c(RGDfK).

Synthesis of 356-AuNPs-c(RGDfK) and 356-AuNRs-c(RGDfK)

According to the literature,[38,39,45] compound YW3-56 was synthesized and purified. YW3-56 was loaded on the surface of gold nanoparticles by nanoprecipitation method.[46] Briefly, 5 mL AuNPs-c(RGDfK) (0.05 mg/mL) or AuNRs-c(RGDfK) (0.05 mg/mL) and 5 mL YW3-56 with different concentrations (0.001 mg/mL, 0.005 mg/mL, 0.01 mg/mL, 0.05 mg/mL and 0.1 mg/mL) were mixed under stirring. The mixture was stirred for another 2 h. After dialyzing in distilled water (to remove unloaded YW3-56), 356-AuNPs -c(RGDfK) or 356-AuNRs-c(RGDfK) was obtained and stored at 4 °C. The solution was concentrated to required drug concentration before use.

In vivo Activity

Female BLAB/C Nude mice and male ICR mice were purchased from Beijing Vital River Laboratory Animal Technology Co., Ltd. The animal study in this work was approved by the Institutional Animal Care and Use Committee of Capital Medical University, and the ethics number is AEEI-2018-174. Humane care of animals was given in the animal studies followed the protocol and the Regulations on Laboratory Animal Welfare issued by Chinese Ministry of Science and Technology.

Sarcoma 180 (S180) cells of 4×10^{6} prepared from one tumor bearing mice were inoculated subcutaneously at right flank of male ICR mice. Treatments were started 5 days after cell implantation, when tumor in the mice reached average volume of 85~100 mm^3. S180 bearing mice were randomly assigned to seven treatment groups, including normal saline (NS), DOX, YW3-56 (356), AuNPs-c-(RGDfK), AuNRs-c(RGDfK), 356-AuNPs-c(RGDfK) and

356-AuNRs-c(RGDfK). The mice of the experimental animals were administered by intravenous (i.v.) injection once a day for one week. The treatment efficacy and safety evaluation were assessed by measuring the tumor volume and body weight, respectively. The tumor dimensions and body weights of mice were measured daily. Tumor volume was calculated by the following formula:

Tumor volume (V) = a^2*b/2 (where a and b are the shortest and the longest diameter, respectively, of a given tumor).

Female BALB/C Nude mice were used to evaluate the chemo-photothermal combined therapy in vivo. A549 cells were subcutaneously injected to form solid tumors. The tumors were implanted by injecting 0.1 mL of normal saline (NS) containing 5×10^6 tumor cells under the skin into the right flank of mice. When the tumor size reached approximately 150 mm^3 in volume (13 days after implantation), the mice were randomly divided into the following treatment groups: NS (i.v., 6 mice), 356 (i.v. dose: 10 μmol/kg/day, 6 mice), AuNRs-c(RGDfK) (i.v. dose: 1 mg/kg/day, 6 mice) and 356-AuNRs-c(RGDfK) (i.v. dose: 1 mg/kg/day NPs and 1 μmol/kg/day 356, 6 mice). The drugs were administered by intravenous injection every day. The mice were irradiated with 808 nm laser (1 w/cm^2) the other day in 7 days after the beginning of the administration. At 30 min after administration, tumor was irradiated for 4 minutes. The weight and volume of mice were detected the other day. 24 h after the last injection, the mice were weighed and killed with ether anesthesia, and the organs and tumor were immediately obtained.

In vivo Biosafety of Chemo-Photothermal Combined Therapy

The tissues of A549 tumor-bearing mice less than 300 mg were digested in H_2O_2 and HNO_3 (1/1) using MARS5 Microwave digestion system. Then fixed volume of the digested liquid to 10 mL with water to determine the content of Au using Agilent Technologies 8800 ICP-MS Triple Quad.

Blood was taken from the eye. The blood used for blood routine examination was added to tubes containing EDTA. Then, blood routine examination was determined by a blood cell analyzer (URIT-5160Vet). The blood used for blood biochemistry was added to tubes without anticoagulant and centrifuged (3000 rpm for 10 min at 4 °C) to obtain the serum. Serum Crea, Urea, ALT and AST levels were measured with a chemistry analyzer and the appropriate reagents (BS-600, Mindray)

Results and Discussion

Characterization of AuNPs-c(RGDfK) and AuNRs-c(RGDfK)

To identify the synthesized gold nanoparticles and their modifier, UV-vis spectrophotometry, TEM and DLS were used. UV-vis absorbance spectra of AuNPs and its modifiers (Figure 1A) showed that the maximum absorption peak shifted from 527 nm to 531 nm after HS-PEG-COOH modification. The maximum absorption peak of AuNPs-c(RGDfK) also presented a slight red shift from 531 nm to 534 nm. And there was a characteristic absorption peak of c(RGDfK) around 258 nm, which was absent in spectrophotometry of AuNPs-PEG-COOH. UV-vis absorbance spectra of AuNRs and its modifiers (Figure 1B) showed that the maximum absorption peak of AuNRs was 758 nm. Same as the change of AuNPs, the horizontal plasmon resonance absorption (TSPR) of AuNRs does not change significantly, and the longitudinal plasmon resonance absorption (LSPR) has a slight red shift from 758 nm to 764 nm after HS-PEG-COOH modification. After cRGD conjugation, the maximum UV-vis absorption peak shifted to 769 nm. Newly emerging peaks 258 nm was also found in the spectrophotometry of AuNRs-c(RGDfK). These changes indicated successful conjugation of PEG and c(RGDfK) peptide.

TEM images (Figure 1C–D) showed that AuNPs/AuNRs and their modifiers were well dispersed with a narrow size distribution. The AuNPs were globular in shape and 30 nm in diameter. The AuNRs exhibited a rod shape with an average aspect ratio of 4.2 (50 nm in length and 12 nm in width). The modification of AuNPs/AuNRs with PEG and conjugation of c(RGDfK) peptide did not change the morphology of the nanoparticles.

Figure 1E showed that the zeta potential of AuNPs was negative charge (−25.2 ± 0.6 mV) due to the use of sodium citrate during the colloidal gold synthesis.[14] When the surface of AuNPs was modified with a long chain structure HS-PEG-COOH molecule and c(RGDfK), the surface maintained a negative value despite the decrease in zeta potential values. Figure 1F showed that the zeta potential of AuNRs was positive charge (20.2 ± 4.0 mV) due to the effect of the cationic nature of cetyltrimethylammonium bromide (CTAB).[47] When CTAB was replaced with HS-PEG-COOH, the zeta potential of AuNRs-PEG shifted in

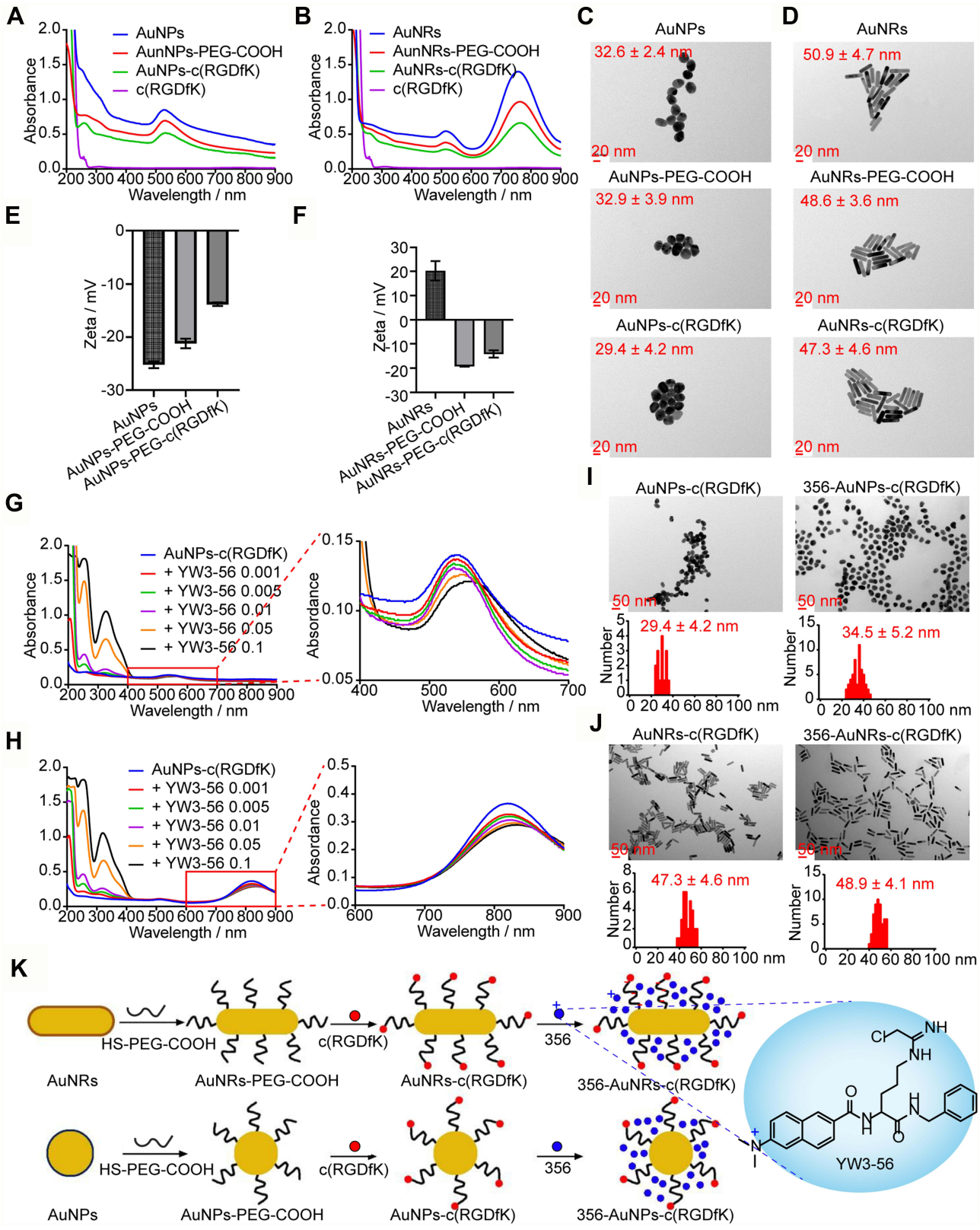

Figure 1 Characterization of Gold nanospheres (AuNPs), nanorods (AuNRs) and their modifiers. (**A**) UV–vis spectra of AuNPs and its modifiers. (**B**) UV–vis spectra of AuNRs and its modifiers. (**C**) TEM images of AuNPs and its modifiers. (**D**) TEM images of AuNRs and its modifiers. (**E**) Zeta potential of AuNPs and its modifiers. (**F**) Zeta potential of AuNRs and its modifiers determined by DLS. (**G** and **H**) Changes in the UV–vis spectra of AuNPs and AuNRs interaction with different concentrations of YW3-56 (0.001 mg/mL, 0.005 mg/mL, 0.01 mg/mL, 0.05 mg/mL and 0.1 mg/mL). (**I** and **J**) TEM images of AuNPs and AuNRs with or without 0.1 mg/mL YW3-56. (**K**) Synthesis scheme of 356-AuNRs-c(RGDfK) and 356-AuNPs-c(RGDfK).

https://doi.org/10.2147/IJN.S319210 DovePress

negative direction to −19.2 ± 0.1 mV due to the carboxyl end group of HS-PEG-COOH molecule dissociated in aqueous solution and showed negative potential. On conjugation with c(RGDfK), zeta potential of AuNRs- c-(RGDfK) shifted a little in positive direction to −14.1 ± 1.5 mV due to slight positive charge of c(RGDfK). The shift in the zeta potential also indicated successful conjugation of PEG and c(RGDfK) peptide.

Characterization of 356-AuNPs-c(RGDfK) and 356-AuNRs-c(RGDfK)

To identify the loading of 356, UV-vis spectrophotometry and TEM were applied. Varying concentrations of YW3-56 (0.001 mg/mL, 0.005 mg/mL, 0.01 mg/mL, 0.05 mg/mL and 0.1 mg/mL) were loaded in AuNPs-c(RGDfK) and AuNRs-c(RGDfK). The characteristic peaks of AuNPs-c(RGDfK) and AuNRs-c(RGDfK) are around 520 nm and 810 nm, respectively. And the peaks around 330 nm was the characteristic peak of YW3-56. With the concentration of 356 increasing, the characteristic peaks of gold NPs were slightly weakened and occurred a red shift while the characteristic peak of YW3-56 was enhanced (Figure 1G and H). This suggested that 356-loaded level was not reached saturation. The loaded amount of 356 absorbed on the surfaces of AuNPs-c(RGDfK) and AuNRs-c(RGDfK) was by subtracting the equilibrium concentration of the drug outside the dialysis bag from the total drug concentration.[48] The concentration of 356 outside the dialysis bags was quantified by a HPLC method (Figure S1). Concentrations of free YW3-56 were below the minimum concentration of 7.8215 μg/mL, which was negligible. In addition, as shown in Table S1, Zeta potential of 356-loaded gold NPs kept stable when 0.025 mg/mL YW3-56 adding to 0.05 mg/mL gold NPs. Thus, we selected 356-loaded gold NPs (w/w = 2:1) to continue to be intensively studied. TEM images in Figures 1I and J and S2 showed that the loading of 0.1 mg/mL 356 did not change the morphology and size of the nanoparticles. As shown in Figure 1K, the driving force for the loading was electrostatic adsorption between 356 and the surfaces of gold nanoparticles.[49–51] In details, YW3-56 was positively charged in aqueous solution because of the nitrogen(+) of the N,N-dimethyl group, while gold nanoparticles were negatively charged as showed by their zeta potential. This led to the formation of YW3-56 and the gold nanoparticles via electrostatic bonding.[52]

In vitro Growth Inhibitory Effect

The in vitro growth inhibitory effect of nanoparticles (NPs) on the S180, 95D, A549 and MCF-7 cancer cells was evaluated using the MTT assay. In order to ensure the comparability of data, the concentrations of 356 and gold nanoparticles in different groups were consistent. Specifically, 20 μM (10 μg/mL) 356 corresponded to 20 μg/mL gold nanoparticles. The cancer cells treated with of 20 μg/mL AuNPs-c(RGDfK) and AuNRs-c(RGDfK) showed 85% to 90% viability (Figure 2A–D). This suggested that the blank NPs were nontoxic at each of the tested concentrations.[53] Figure 2A–D indicated that the growth inhibitory effect of 356-AuNRs-c(RGDfK) and 356-AuNPs-c(RGDfK) on the S180, 95D, A549 and MCF-7 cancer cell was slightly higher than that of free 356. Figure 2E showed the IC_{50} value of 356-AuNRs-c-(RGDfK) on lung cancer cells showed 3 folds decrease in IC_{50} value comparable to the pure drug while that of 356-AuNPs-c(RGDfK) showed 2 folds decrease. These results suggested that 356-loaded NPs could improve the growth inhibitory effect. However, there was no significant difference in terms of anti-tumor activity on S180 and MCF-7 cells for the two 356-loaded NPs.

Thus, A549 cells was selected to evaluate the cytotoxicity of conjugated AuNRs with 808 nm laser irradiation. The viability of A549 cells exposure to 808 nm laser irradiation and incubation with 1.0 μg/mL AuNRs-c(RGDfK) have a significant decrease, while no decrease in cell viability was observed with laser irradiation or incubation with AuNRs-c(RGDfK) alone (Figure 2F). Although 356-AuNRs-c(RGDfK) could delay tumor growth with or without laser irradiation, there are still significant differences before and after laser irradiation. As shown in Figure S3, the ratio of dead cells increased significantly after laser irradiation compared with that without laser irradiation. This suggested that laser irradiation added to 356-AuNRs-c(RGDfK) could improve the anti-tumor activity of nanodrug in vitro. The stability of 356-AuNRs-c(RGDfK) was detected by UV-vis spectrum as shown in Figure S4. 2 w/cm^2 laser was irradiated for different time and the UV-vis spectra had no change during or after irradiation. And the UV-Vis spectra kept stable while the UV absorption peaks appeared to blue shift with pH decreasing. This indicated that 356-AuNRs -c(RGDfK) could keep stable with irradiation in physiological environment and could release 356 in the tumor environment.

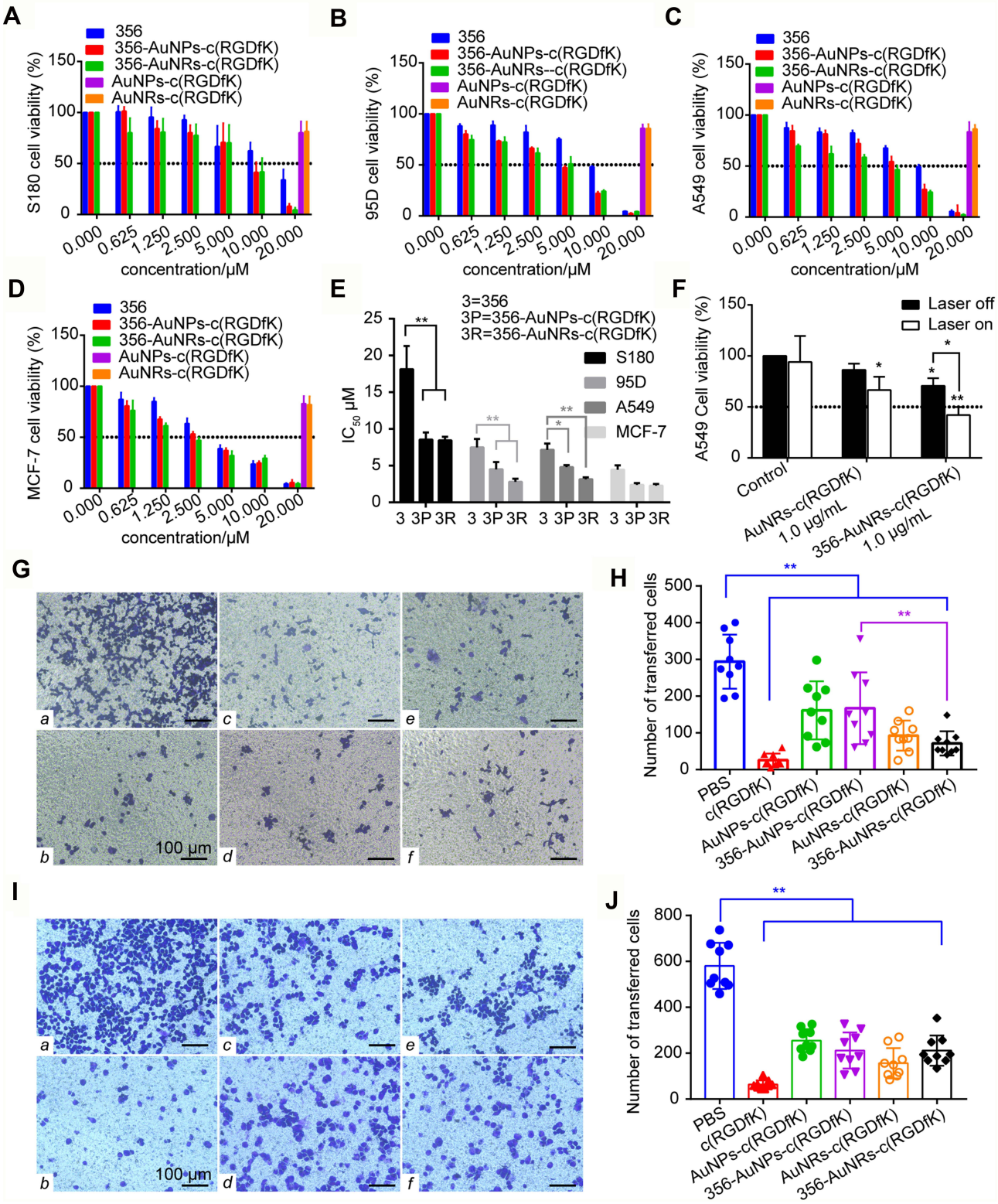

Figure 2 In vitro activity. (**A**–**D**) Cell viability of S180, 95D, A549 and MCF-7 cells treated with different concentration nanodrugs. The concentration marked on the figure was that of 356 and 20 μM 356-loaded gold NPs were equal to 20 μg/mL gold NPs. (**E**) IC_{50} of 356, 356-AuNPs-c(RGDfK) and 356-AuNRs-c(RGDfK) on S180, 95D, A549 and MCF-7 cells. (**F**) Cell viability of control, AuNRs-c(RGDfK) and 356-AuNRs-c(RGDfK) on A549 cells with or without 808 nm Laser irritation for 1 min (2 w/cm^2). (**G**–**J**) Representative images and analysis of anti-metastatic activity and anti-invasive activity. a: PBS, b: c(RGDfK), c: AuNPs-c(RGDfK), d: 356-AuNPs-c(RGDfk), e: AuNRs-c(RGDfK), f: 356-AuNRs-c(RGDfK). * represents $p < 0.05$, ** represents $p < 0.01$.

Anti-Invasive and Anti-Metastatic Effect on A549 Cells

To determine the antimetastatic and anti-invasive ability of NPs in vitro, the transwell assay and Matrigel invasion assay were conducted. Figure 2G and H showed that the number of A549 cells passing through the transwell membrane pores decreased significantly after NPs incubation. And Figure 2I and J illustrated that 1.0 μg/mL NPs also inhibited the invasiveness of these cells. This could be due to the introduction of c(RGDfK).[43,54] The cells treated with 356-AuNRs-c(RGDfK) have higher antimetastatic ability compared with those treated with 356-AuNPs -c(RGDfK).

Cellular Uptake and Colocalization

As shown in Figure 3A and B, compared to control group, faint blue fluorescence (403/462) was detected in the cell area of 356 treated group, and indicated that 365 (4 μM) was not easy to penetrate through cell membranes to be taken up. However, the brighter blue fluorescence was observed in 356-AuNRs-c(RGDfK) and 356-AuNPs-c-(RGDfK) group. This indicated that 356-AuNRs-c-(RGDfK) and 356-AuNPs-c(RGDfK) entered A549 cells effectively.

The amount of histone H3 citrullination was analyzed using anti-histone H3cit antibody (Alexa Fluor 647). The staining revealed strong nuclear labeling in the A549 cells treated with PBS, which was less diffuse in the groups of free 356 and NPs. Notably, 356-AuNRs-c(RGDfK) and 356-AuNPs-c(RGDfK) were able to significantly inhibit the histone H3 citrullination by analyzing the intensity of red fluorescence (Figure 3C). The results showed that 356 modification with NPs could significantly increase the inhibition of PAD4 activity. This might be attributed to the fact that drug-loaded NPs could deliver 356 more efficiently into the cells.

Uptake Pathway Determination

To further investigate potential endocytic mechanisms for 356-AuNRs-c(RGDfK) and 356-AuNPs-c(RGDfK), some selective inhibitors chlorpromazine (CPZ), amiloride hydrochloride (AM) and methyl-β-cyclodextrin (Mβ-CD) were used to check the effects on the uptake efficiency of NPs. First, none of these inhibitors affected the cell viability.[55] After pre-incubation with the individual inhibitor, cells were co-cultured with NPs for another 2 h. As shown in Figures 3D and S5, the uptake of 356 and 356-loaded NPs decreased slightly after the pre-treatment with chlorpromazine and amiloride hydrochloride, which could specifically inhibit the clathrin-mediated endocytosis and macrocytosis-mediated endocytosis, respectively. In the presence of a specific caveolin-mediated endocytosis inhibitor (Mβ-CD), the internalization efficiencies of 356 and 356-loaded NPs were markedly reduced. Specifically, the internalization of 356 and 356-loaded NPs exhibited an inhibition rate of approximately 80% in A549 cells. The results indicated that 356 entered the cell through specific caveolin-mediated endocytosis. The nanoparticles did not affect the way of uptake.

In vivo Anti-Tumor Activity on S180-Bearing Mice

The anti-tumor activity of NPs on the same dose (356: 10 μmol/kg, 356-loaded NPs containing 1 μmol/kg 356 and 1 mg/kg NPs, NPs: 1 mg/kg) was examined on S180-bearing mice model. Figure 4A showed that 356 and 356-loaded NPs could inhibit the growth of S180 sarcoma. And there was no significant inhibition effect in the AuNPs-c(RGDfK) and AuNRs-c(RGDfK) groups. This suggested that 356-loaded NPs showed enhanced anti-tumor activity compared to the NPs alone and the anti-tumor effect of 356-loaded NPs was consistent with 10-fold free drug 356.

Distribution of 356 and 356-loaded NPs in Tumor Tissues and Its Effect on H3cit

The pictures in Figure 4D showed that 356 and 356-loaded NPs with blue fluorescence aggregated in the tumor tissue. The analysis in Figure 4C illustrated that the mean fluorescence intensity of 356-AuNRs-c(RGDfK) increased significantly in comparison with that of free drug 356. In addition, the expression of H3cit in tumor tissue sections was observed by analyzed the mean fluorescence intensity of red fluorescence area. Figure 4B showed that red fluorescence intensity in 356 and 356-loaded NPs groups all decreased and there was no significant difference between 10 μmol/kg 356 group and 356-loaded NPs groups (including 1 μmol/kg 356). This indicated that 356 and 356-loaded NPs could significantly inhibit the histone H3 citrullination in tumor tissues. This was consistent with the results in vitro.

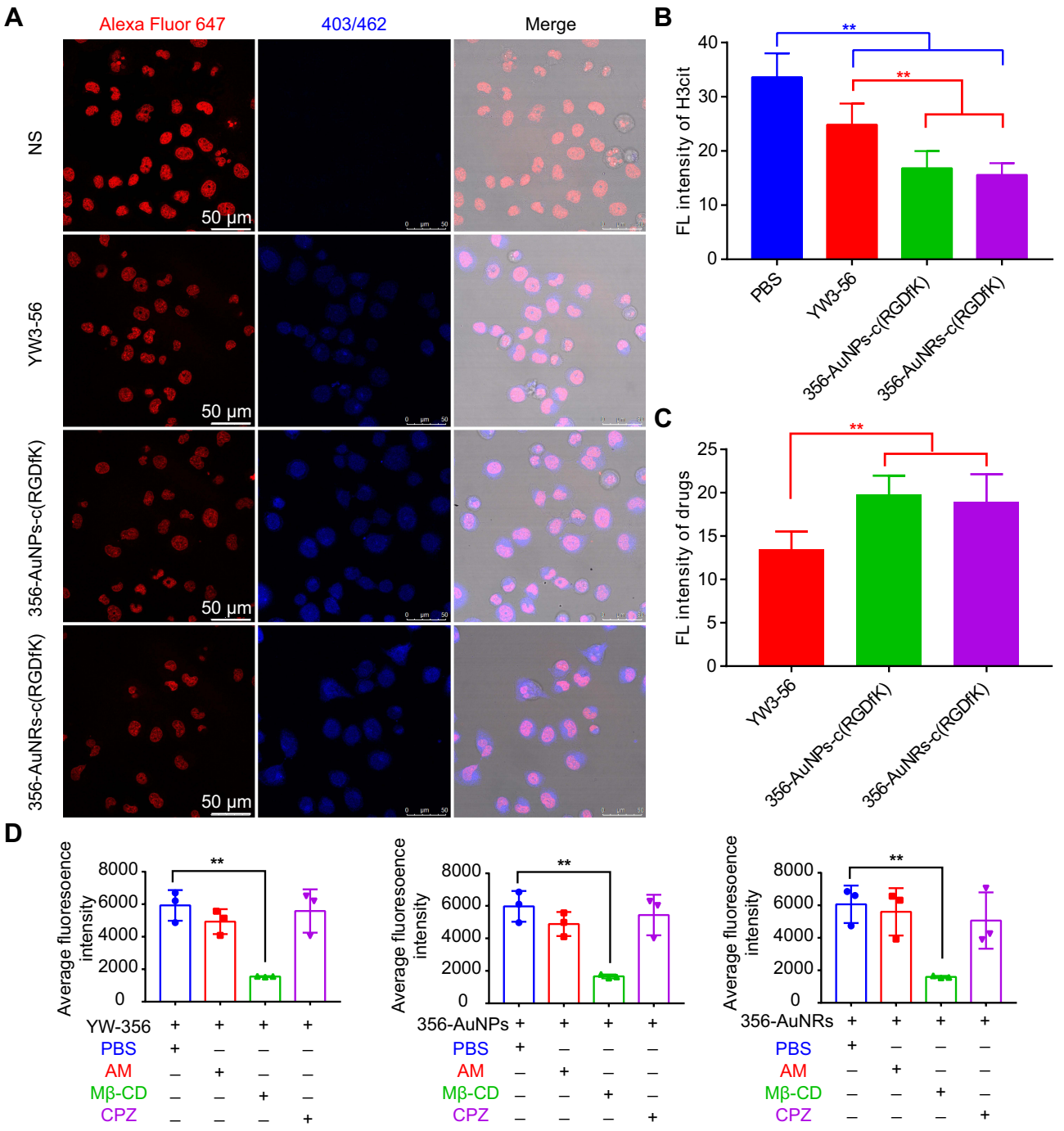

Figure 3 The internalization and pathway of NPs into A549 cells. (**A**) Representative images showing cellular uptake of 356 and the H3cit protein colocalization with 356. (**B** and **C**) Analysis of histone H3 citrullination and uptake of 356 and 356-loaded NPs in A549 cells. (**D**) Uptake pathway determination of 356 and 356-loaded NPs. ** represents $p < 0.01$.

In vivo Chemo-Photothermal Combined Therapy on A549 Tumor-Bearing Mice

In comparison with chemotherapy alone, the combined chemo-photothermal therapy exhibited a synergistic effect, resulting in even higher therapeutic efficacy.[56,57] Thus, NPs treatment combined 808 nm laser irradiation was conducted on BALB/C Nude mice implanted with A549 tumor. The tumor weight (Figure 5A) showed that 10 μmol/kg 356, AuNRs-c(RGDfK) and 356-AuNRs-c-(RGDfK) were able to inhibit tumor growth significantly after 22 days combined treatment. Although 356-AuNRs -c(RGDfK) only contained 1 μmol/kg 356, it has higher

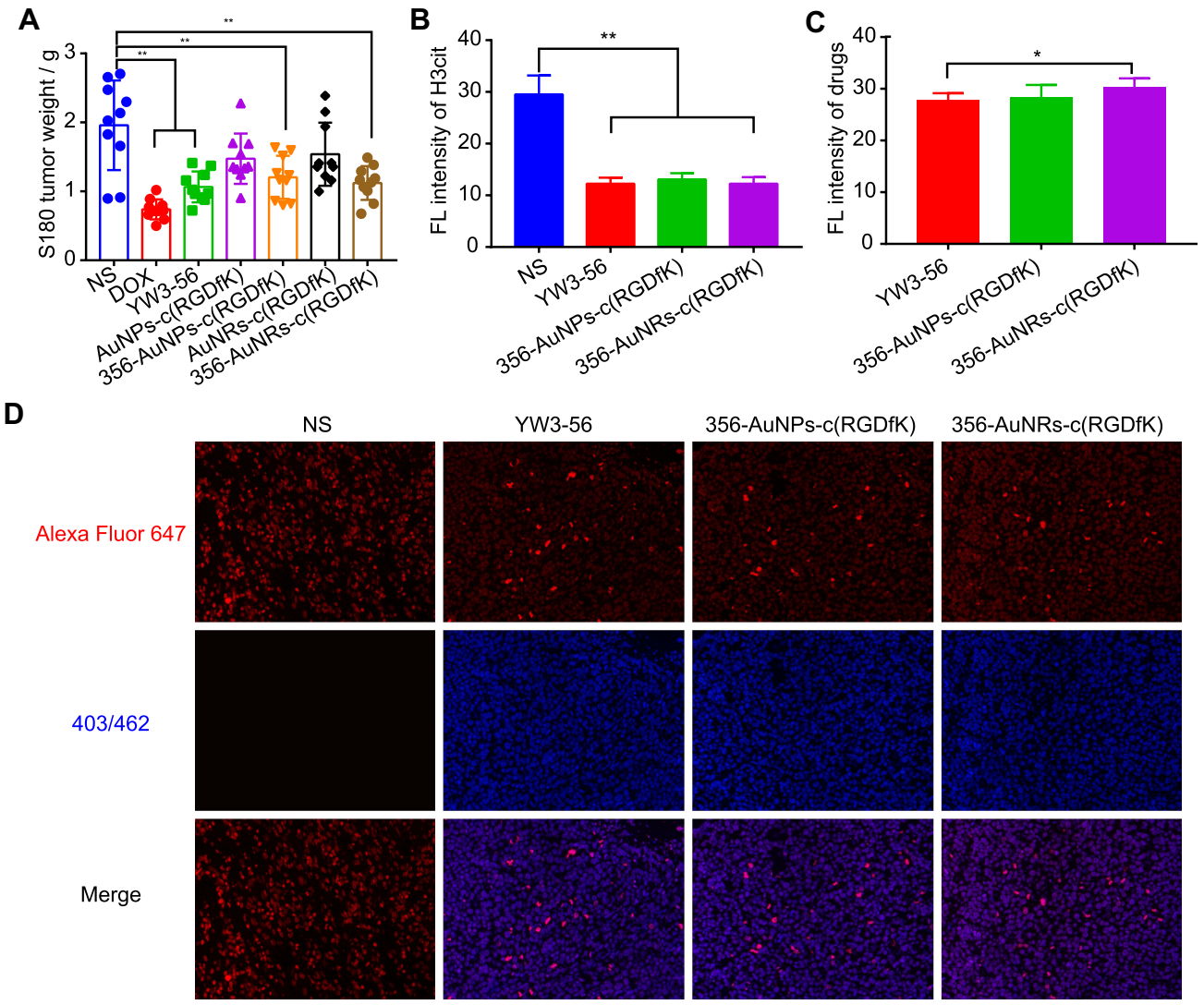

Figure 4 In vivo anti-tumor activity on S180 tumor-bearing mice of 356 and 356-loaded NPs (YW3-56: 10 μmol/kg, 356-loaded NPs containing 1 μmol/kg 356 and 1 mg/kg NPs, NPs: 1 mg/kg). (**A**) The weight of S180 tumor. (**B** and **C**) Analysis of histone H3 citrullination and distribution of 356 and 356-loaded NPs in tumor tissues. (**D**) Representative pictures of H3 citrullination immunofluorescence and distribution of 356 and 356-loaded NPs. * represents $p < 0.05$, ** represents $p < 0.01$.

therapeutic efficacy than 10 μmol/kg 356. During the treatment, the tumor volumes were monitored every other day (Figure 5B). Compared to the NS group, all groups could decrease the volumes. The mean tumor volume of 356-AuNRs-c(RGDfK) group on 2nd day after irradiation was significantly smaller than that of the saline group. And the difference in tumor volume between the other groups and control group was seen on the fifth day after irradiation. After 22 days treatment, the tumor volume of the chemotherapy group (356 group) was similar to that of the photothermal treatment group (AuNRs-c(RGDfK) group). However, they were both significantly larger than that of the combined treatment group (356-AuNRs-c(RGDfK) group). In addition, the mice weight exhibited normal increasing trends and there was no difference among all groups (Figure 5C).

Temperature changes on tumor sites of mice were recorded and analyzed at various time points after laser irradiation (Figure 5D). After laser irradiation for 4 min, the tumor site temperature of NS group mice only increased by 9.1 °C, while that of AuNRs-c(RGDfK) and 356-AuNRs-c-(RGDfK) groups mice increased by 15.7 °C and 18.9 °C, respectively. And no difference was observed between 356 group and NS group. In the 2nd minute of laser irradiation, the

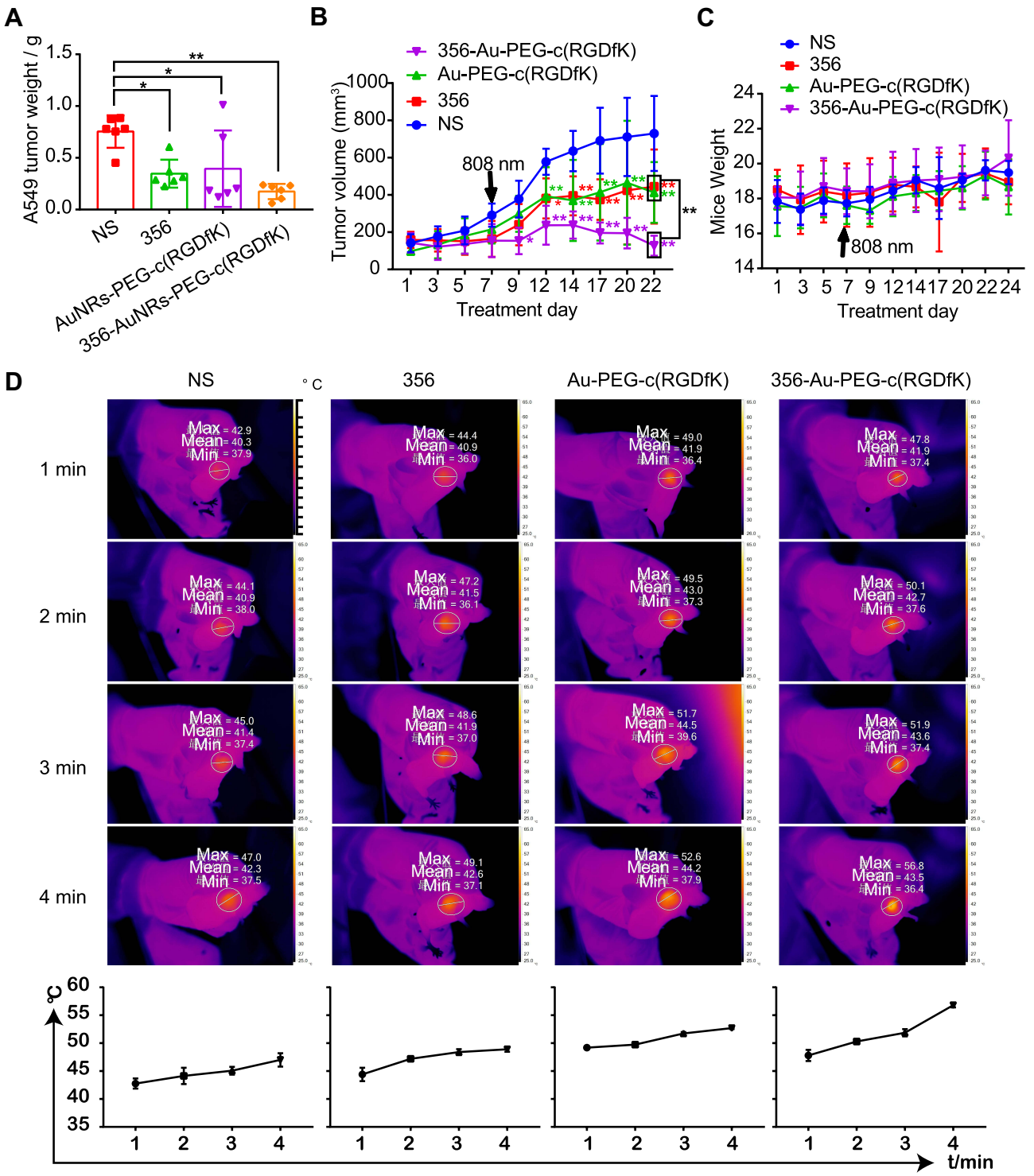

Figure 5 Chemo-photothermal combined therapy of 356 and 356-loaded NPs (356: 10 μmol/kg, 356-AuNRs-c(RGDfK) containing 1 μmol/kg 356 and 1 mg/kg AuNRs-c(RGDfK), AuNRs-c(RGDfK): 1 mg/kg) (**A**) The weight of A549 tumor. (**B**) Tumor volume changes of the mice during the administration period. (**C**) Changes in body weight during the administration period. (**D**) The representative pictures showing temperature changes at the tumor sites during laser irradiation and average temperature changes of the tumor sites. Pictures were taken at the ninth day of drug administration. * represents $p < 0.05$, ** represents $p < 0.01$.

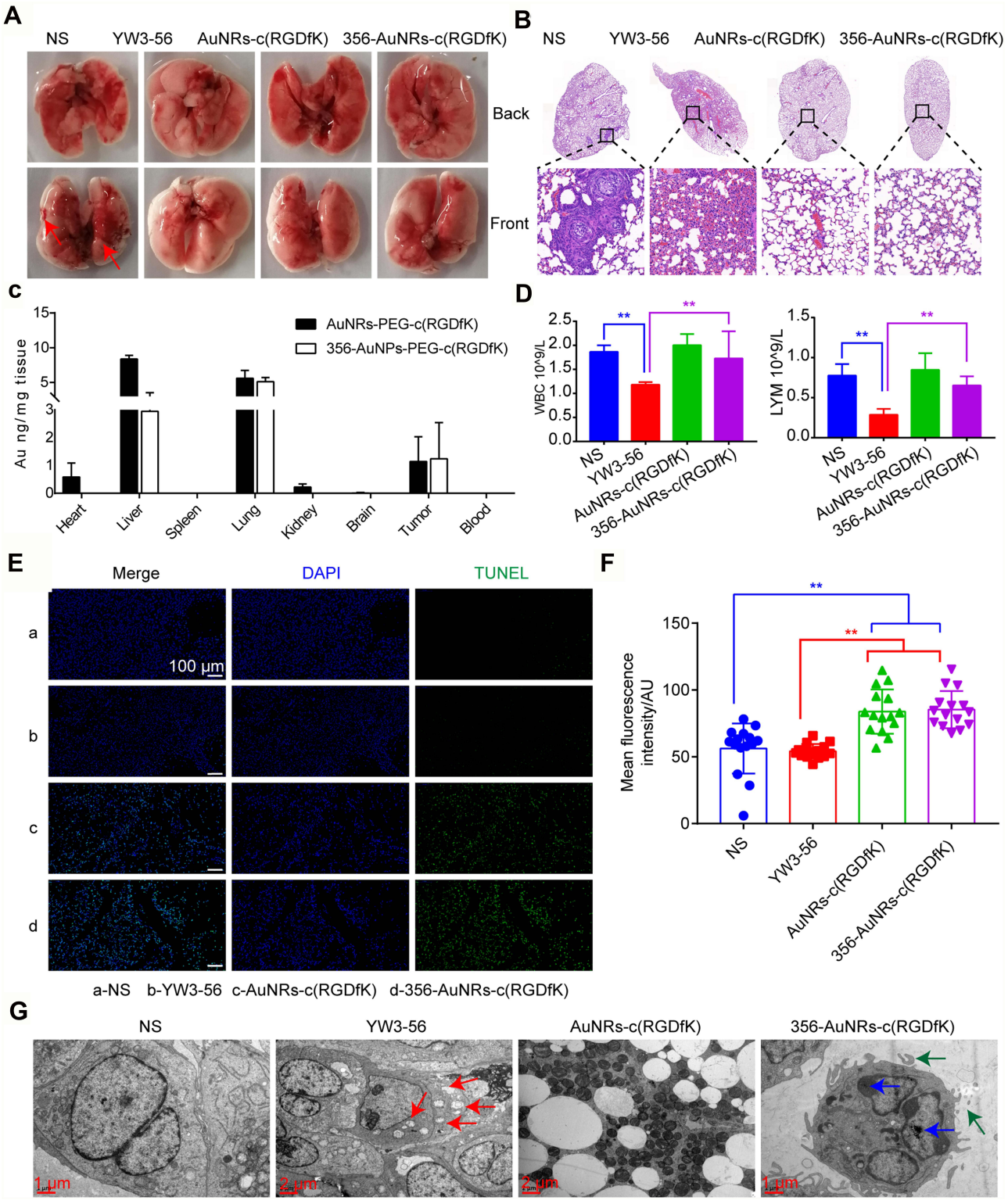

Figure 6 (**A**) Representative photographs of lungs. (**B**) HE Staining for the lungs of tumor-bearing mice. (**C**) Gold content in heart, liver, spleen, lung, kidney, brain, tumor and blood tissues measured by ICP-MS. (**D**) The count of WBC and LYM determined by a blood cell analyzer. (**E** and **F**) Representative images and statistical analysis of apoptosis in tumor tissue determined by TUNEL assay. (**G**) Representative TEM pictures of tumor tissue. ** represents $p < 0.01$.

tumor site temperature of the mice treated with AuNRs-c-(RGDfK) and 356-AuNRs-c(RGDfK) increased to more than 50 °C. These results indicated that the 356 loading of AuNRs-c(RGDfK) did not affect its photo-thermal conversion.

Lung Metastasis

Lung metastasis was observed by lung photographs and lung H&E staining from A549 tumor-bearing mice (Figure 6A and B). Lung photographs showed that there were macroscopically visible metastatic nodules on the lungs' surface of the mice injected with normal saline. At the meantime, microscopically visible nodules could be observed by H&E staining. Furthermore, visible metastatic nodules did not be observed in 356 treatment group. However, a marked infiltration of inflammatory cells surrounding blood vessels was observed in lung H&E sections. Compared with the NS and 356 groups, lung tissue sections of mice in AuNRs-c(RGDfK) and 356-AuNRs -c(RGDfK) groups displayed normal alveolar architecture and no inflammatory cells.

In vivo Biosafety of Chemo-Photothermal Combined Therapy

To evaluate the biosafety of these nanodrugs, Au accumulation in various tissues of A549 tumor-bearing mice was determined by ICP-MS (Figure 6C). After 356 loading, the Au content in heart, kidney and brain disappeared compared with the AuNRs-c(RGDfK) and that in liver decreased approximately to the one-third of Au content in AuNRs-c(RGDfK) group. However, the level of Au content in tumor tissues and lung tissues did not change a lot. This suggested that 356 loading reduced liver and kidney injuries caused by gold accumulation in other organs. This may be related to the rapid metabolism of 356. In addition, no obvious histopathological changes were observed in heart, kidney, liver and spleen section (Figure S6A).

Blood biochemistry and blood routine examination were also conducted to evaluate the biosafety of these nanodrugs in vivo. Figure 6D showed that 356 significantly decreased white blood cells (WBC) and lymphocyte (LYM) count. However, 356-loaded AuNRs-c(RGDfK) increased the level of these two parameters which may be due the decrease in the dose of chemotherapy. In addition, Figure S6B–D showed no significant difference between NS group and treatment groups in blood biochemistry parameters, the count of red blood cells (RBC) and platelet (PLT). This illustrated that the nanodrugs did not cause liver/kidney injury, hemolysis, and thrombus. These results were consistent with that previously reported.[39]

Tumor-Suppressive Mechanisms of Chemo-Photothermal Combined Therapy in vivo

When the tumor site of mice received photothermal agents and NIR irradiation, apoptosis and necrosis were induced in tumor tissues.[58,59] TUNEL staining was used to detected apoptosis (Figure 6E and F). There were few apoptotic cells (TUNEL-positive cells) in NS and 356 groups. However, the number of apoptotic tumor cells in AuNRs-c(RGDfK) and 356-AuNRs-c(RGDfK) treatment groups were significantly increased compared with that in NS and 356 groups. This suggested that laser-induced apoptosis may be one of the reasons that photothermal therapy inhibited the growth of A549 tumors.

The apoptosis and necrosis of tumor tissues also were determined by TEM (Figure 6G). Ultrastructure of the normal tumor cells was complete, nuclear membrane was clear and mitochondrial structure was intact. Many autophagosomes (red arrows) were accumulated in the cytoplasm of tumor cells treated with 356, which was consistent with the literature reported previously.[45] The tumor tissues in AuNRs-c(RGDfK) treatment group demonstrated a marked appearance of necrosis while those in 356-AuNRs-c(RGDfK) treatment group occurred apoptosis. Cytoplasmic vacuolization and increasing mitochondria were observed in tumor tissues of AuNRs-c-(RGDfK) and nuclear construction disappeared. Apoptotic bodies (green arrows) formed around the cell membrane and the chromatin accumulated along the nuclear membrane in tumor tissues of 356-AuNRs-c-(RGDfK) treatment group. In addition, the gold nanoparticles were found to be distributed in the nucleus (blue arrows).

Through the above experiments, we found that 356-AuNRs-c(RGDfK) triggered apoptosis higher than necrosis while AuNRs-c(RGDfK) preferred to induce necrosis. This suggested that the introduction of 356 to AuNRs-c(RGDfK) may manage the scar formed around the treated tumor.

Conclusion

In this work, we constructed RGD targeting and PAD4 inhibitor loading gold nanospheres and nanorods. And the

356-loaded NPs had enhanced the cell killing ability in vitro compared with 356 alone or NPs alone. They also exhibited the ability to resist metastasis and invasion in vitro due to RGD functional modification of the NPs surface. Compared with the 356 alone group, the better penetration for tumor cells and tissues of 356-loaded NPs was improved. And the inhibition of histone citrullination in cells was significantly strengthened while the uptake pathway in cells was not affected.

We found that the activity of 356-AuNRs-c(RGDfK) were better than that of 356-AuNPs-c(RGDfK) in vitro and in vivo, including in vitro cell killing ability with or without laser irradiation, anti-metastatic activity, and tissue intake. Thus, 356-AuNRs-c(RGDfK) was selected to evaluate activity of chemo-photothermal combined therapy. Firstly, we used infrared cameras to find that 356 loading did not affect the photothermal conversion ability of gold nanorods in vivo. By monitoring the changes of tumor volume and tumor weight, we found that the anti-tumor effect of 356-AuNRs-c(RGDfK) was significantly enhanced and the dosage of 356 was reduced. Secondly, photographs of the lungs and analysis of lung H&E sections showed that 356-AuNRs-c(RGDfK) also inhibited tumor metastasis and inflammatory infiltration in the lungs. Thirdly, after 356 loading, the accumulation of gold in heart, liver, lung and kidney decreased or even disappeared, but did not affect the accumulation of gold in tumor. This may be due to the fact that rapid metabolism of 356 affects that of gold nanorods. In addition, blood routine test showed that 356 caused a decrease in white blood cells and lymphocytes, while 356-AuNRs-c(RGDfK) did not. It may possibly be related to a decrease in 356 doses. Finally, we found that both AuNRs-c(RGDfK) and 356-AuNRs-c(RGDfK) could cause apoptosis in tumor tissue. This was consistent with the research previously. However, how 356 affected the metabolism of gold nanorods requires further study. Overall, the combination therapy of 356-loaded NPs with PTT is a good strategy for addressing miss effects and biotoxicity of PAD4 inhibitors.

Abbreviations

TEM, transmission electron microscopy; NPs, gold nanoparticles; AuNPs, gold nanospheres; AuNRs, gold nanorods; I/R, ischemia-reperfusion; NETs, neutrophil extracellular traps, RA, rheumatoid arthritis; TUNEL, TdT-mediated dUTP Nick-End Labeling; H3cit, citrullination of histone 3; PAD4, peptidyl arginine deiminase 4; PTT, photothermal therapy; H&E, hematoxylin-eosin staining; WBC, white blood cells; LYM, lymphocyte; RBC, red blood cells; PLT, platelet.

Data Sharing Statement

The data that support the findings of this study are available from the corresponding author upon reasonable request.

Ethics Approval and Informed Consent

Male ICR mice were purchased from Beijing Vital River Laboratory Animal Technology Co., Ltd. The study was approved by the Institutional Animal Care and Use Committee of Capital Medical University, and the ethics number is AEEI-2018-174. Humane care of animals was given in the animal studies followed the protocol and the Regulations on Laboratory Animal Welfare issued by Chinese Ministry of Science and Technology.

Consent for Publication

The details of any images, videos, recordings, etc can be published. All authors have given approval to the final version of the manuscript.

Author Contributions

All authors made a significant contribution to the work reported, whether that is in the conception, study design, execution, acquisition of data, analysis and interpretation, or in all these areas; took part in drafting, revising or critically reviewing the article; gave final approval of the version to be published; have agreed on the journal to which the article has been submitted; and agree to be accountable for all aspects of the work.

Funding

This work was supported by the Beijing Municipal Colleges and Universities High Level Talents Introduction and Cultivate Project-Beijing Great Wall Scholar Program (CIT&TCD 20180332).

Disclosure

The authors report no conflicts of interest in this work.

References

1. Koushik S, Joshi N, Nagaraju S, et al. PAD4: pathophysiology, current therapeutics and future perspective in rheumatoid arthritis. *Expert Opin Ther Tar.* 2017;21:433–447. doi:10.1080/14728222.2017.1294160

2. Mondal S, Thompson PR. Protein arginine deiminases (pads): biochemistry and chemical biology of protein citrullination. *Accounts Chem Res*. 2019;52:818–832. doi:10.1021/acs.accounts.9b00024
3. ScienceDirect. *Clin Microbiol Newsl*. 2015;37(4):33. doi:10.1016/j.clinmicnews.2015.01.008
4. Wang Y. Human PAD4 regulates histone arginine methylation levels via demethylimination. *Science*. 2004;306:279–283. doi:10.1126/science.1101400
5. Alghamdi M, Al Ghamdi KA, Khan RH, Uversky VN, Redwan EM. An interplay of structure and intrinsic disorder in the functionality of peptidylarginine deiminases, a family of key autoimmunity-related enzymes. *Cel Mol Life Sci*. 2019;76:4635–4662. doi:10.1007/s00018-019-03237-8
6. Kang L, Yu H, Yang X, et al. Neutrophil extracellular traps released by neutrophils impair revascularization and vascular remodeling after stroke. *Nat Commun*. 2020;11:1–15. doi:10.1038/s41467-020-16191-y
7. Du M, Yang L, Gu J, Wu J, Ma Y, Wang T. Inhibition of peptidyl arginine deiminase-4 prevents renal ischemia-reperfusion-induced remote lung injury. *Mediat Inflamm*. 2020;2020:1–14.
8. Rabadi MM, Han SJ, Kim M, D'Agati V, Lee HT. Peptidyl arginine deiminase-4 exacerbates ischemic AKI by finding NEMO. *Am J Physiol Renal Physiol*. 2019;316:F1180–F1190. doi:10.1152/ajprenal.00089.2019
9. Teijeira Á, Garasa S, Gato M, et al. CXCR1 and CXCR2 chemokine receptor agonists produced by tumors induce neutrophil extracellular traps that interfere with immune cytotoxicity. *Immunity*. 2020;52:856–871. doi:10.1016/j.immuni.2020.03.001
10. Curran AM, Naik P, Giles JT, Darrah E. PAD enzymes in rheumatoid arthritis: pathogenic effectors and autoimmune targets. *Nat Rev Rheumatol*. 2020;16:301–315. doi:10.1038/s41584-020-0409-1
11. Albrengues J, Shields MA, Ng D, et al. Neutrophil extracellular traps produced during inflammation awaken dormant cancer cells in mice. *Science*. 2018;361:o4227. doi:10.1126/science.aao4227
12. Aliko A, Kamińska M, Falkowski K, et al. Discovery of novel potential reversible peptidyl arginine deiminase inhibitor. *Int J Mol Sci*. 2019;20:2174. doi:10.3390/ijms20092174
13. Nemmara VV, Subramanian V, Muth A, et al. The development of benzimidazole-based clickable probes for the efficient labeling of cellular protein arginine deiminases (PADs). *ACS Chem Biol*. 2018;13:712–722. doi:10.1021/acschembio.7b00957
14. Wang Y, Li P, Wang S, et al. Anticancer peptidylarginine deiminase (PAD) inhibitors regulate the autophagy flux and the mammalian target of rapamycin complex 1 activity. *J Biol Chem*. 2012;287:25941–25953. doi:10.1074/jbc.M112.375725
15. Zhang P, Wang J, Huang H, et al. Unexpected high photothemal conversion efficiency of gold nanospheres upon grafting with two-photon luminescent ruthenium(II) complexes: a way towards cancer therapy? *Biomaterials*. 2015;63:102–114. doi:10.1016/j.biomaterials.2015.06.012
16. Wang W, Guo Z, Lu Y, et al. Receptor-mediated and tumor-microenvironment combination-responsive Ru nanoaggregates for enhanced cancer phototheranostics. *ACS Appl Mater Inter* 2019;11:17294–17305. doi:10.1021/acsami.9b04531
17. Zhang R, Fan X, Meng Z, et al. Renal clearable Ru-based coordination polymer nanodots for photoacoustic imaging guided cancer therapy. *Theranostics*. 2019;9:8266–8276. doi:10.7150/thno.36986
18. Yang S, Zhou L, Su Y, Zhang R, Dong C. One-pot photoreduction to prepare NIR-absorbing plasmonic gold nanoparticles tethered by amphiphilic polypeptide copolymer for synergistic photothermal-chemotherapy. *Chin Chem Lett*. 2019;30:187–191. doi:10.1016/j.cclet.2018.02.015
19. Zhao S, Zhu X, Cao C, Sun J, Liu J. Transferrin modified ruthenium nanoparticles with good biocompatibility for photothermal tumor therapy. *J Colloid Interf Sci*. 2018;511:325–334. doi:10.1016/j.jcis.2017.10.023
20. Liu Y, Bhattarai P, Dai Z, et al. Photothermal therapy and photoacoustic imaging via nanotheranostics in fighting cancer. *Chem Soc Rev*. 2019;7:2053–2108.
21. Hosseini V, Mirrahimi M, Shakeri-Zadeh A, et al. Multimodal cancer cell therapy using Au@Fe2O3 core–shell nanoparticles in combination with photo-thermo-radiotherapy. *Photodiagn Photodyn*. 2018;24:129–135. doi:10.1016/j.pdpdt.2018.08.003
22. Asadi M, Beik J, Hashemian R, et al. MRI-based numerical modeling strategy for simulation and treatment planning of nanoparticle-assisted photothermal therapy. *Physica Medica*. 2019;66:124–132. doi:10.1016/j.ejmp.2019.10.002
23. Alamzadeh Z, Beik J, Mirrahimi M, et al. Gold nanoparticles promote a multimodal synergistic cancer therapy strategy by co-delivery of thermo-chemo-radio therapy. *Eur J Pharm Sci*. 2020;145:105235. doi:10.1016/j.ejps.2020.105235
24. Abed Z, Beik J, Laurent S, et al. Iron oxide–gold core–shell nanotheranostic for magnetically targeted photothermal therapy under magnetic resonance imaging guidance. *J Cancer Res Clin*. 2019;145:1213–1219. doi:10.1007/s00432-019-02870-x
25. Beik J, Asadi M, Khoei S, et al. Simulation-guided photothermal therapy using MRI-traceable iron oxide-gold nanoparticle. *J Photochem Photobiol B: Biol*. 2019;199:111599. doi:10.1016/j.jphotobiol.2019.111599
26. Movahedi MM, Mehdizadeh A, Koosha F, et al. Investigating the photo-thermo-radiosensitization effects of folate-conjugated gold nanorods on KB nasopharyngeal carcinoma cells. *Photodiagn Photodyn*. 2018;24:324–331. doi:10.1016/j.pdpdt.2018.10.016
27. Cheng Z, Zhang T, Wang W, et al. D-A-D structured selenadiazolesbenzothiadiazole-based near-infrared dye for enhanced photoacoustic imaging and photothermal cancer therapy. *Chin Chem Lett*. 2021;32:1580–1585. doi:10.1016/j.cclet.2021.02.017
28. Zhang L, Su H, Wang H, et al. Tumor chemo-radiotherapy with rod-shaped and spherical gold nano probes: shape and active targeting both matter. *Theranostics*. 2019;9:1893–1908.
29. Peralta DV, Heidari Z, Dash S, Tarr MA. Hybrid paclitaxel and gold nanorod-loaded human serum albumin nanoparticles for simultaneous chemotherapeutic and photothermal therapy on 4T1 breast cancer cells. *ACS Appl Mater Inter*. 2015;7:7101–7111. doi:10.1021/acsami.5b00858
30. Manivasagan P, Bharathiraja S, Santha Moorthy M, et al. Anti-EGFR antibody conjugation of fucoidan-coated gold nanorods as novel photothermal ablation agents for cancer therapy. *ACS Appl Mater Inter*. 2017;9:14633–14646. doi:10.1021/acsami.7b00294
31. Ali MRK, Wu Y, Tang Y, et al. Targeting cancer cell integrins using gold nanorods in photothermal therapy inhibits migration through affecting cytoskeletal proteins. *Proc Nat Acad Sci*. 2017;114:E5655–E5663. doi:10.1073/pnas.1703151114
32. Pérez-Hernández M, Del Pino P, Mitchell SG, et al. Dissecting the molecular mechanism of apoptosis during photothermal therapy using gold nanoprisms. *ACS Nano*. 2015;9:52–61. doi:10.1021/nn505468v
33. Melamed JR, Edelstein RS, Day ES. Elucidating the fundamental mechanisms of cell death triggered by photothermal therapy. *ACS Nano*. 2015;9:6–11. doi:10.1021/acsnano.5b00021
34. Liu Y, Wang Z, Liu Y, et al. Suppressing nanoparticle-mononuclear phagocyte system interactions of two-dimensional gold nanorings for improved tumor accumulation and photothermal ablation of tumors. *ACS Nano*. 2017;11:10539–10548. doi:10.1021/acsnano.7b05908
35. Albanese A, Tang PS, Chan WC. The effect of nanoparticle size, shape, and surface chemistry on biological systems. *Annu Rev Biomed Eng*. 2012;14:1–16. doi:10.1146/annurev-bioeng-071811-150124
36. Yang Z, Tian R, Wu J, et al. Impact of semiconducting perylene diimide nanoparticle size on lymph node mapping and cancer imaging. *ACS Nano*. 2017;11:4247–4255. doi:10.1021/acsnano.7b01261

37. Cooper J, Giancotti FG. Integrin signaling in cancer: mechanotransduction, stemness, epithelial plasticity, and therapeutic resistance. *Cancer Cell*. 2019;35:347–367. doi:10.1016/j.ccell.2019.01.007
38. Alipour M, Baneshi M, Hosseinkhani S, et al. Recent progress in biomedical applications of RGD-based ligand: from precise cancer theranostics to biomaterial engineering: a systematic review. *J Biomed Mater Res A*. 2020;108:839–850. doi:10.1002/jbm.a.36862
39. Zhang L, Su H, Cai J, et al. A multifunctional platform for tumor angiogenesis-targeted chemo-thermal therapy using polydopamine-coated gold nanorods. *ACS Nano*. 2016;10:10404–10417. doi:10.1021/acsnano.6b06267
40. Katsamakas S, Chatzisideri T, Thysiadis S, Sarli V. RGD-mediated delivery of small-molecule drugs. *Future Med Chem*. 2017;9:579–604. doi:10.4155/fmc-2017-0008
41. Mahmoudi R, Ashraf Mirahmadi-Babaheidri S, Delaviz H, et al. RGD peptide-mediated liposomal curcumin targeted delivery to breast cancer cells. *J Biomater Appl*. 2021;35:743–753. doi:10.1177/0885328220949367
42. Wu Z, Huang Z, Yin G, et al. RGD/CTX-conjugated multifunctional Eu-Gd 2 O 3 NRs for targeting detection and inhibition of early tumor. *J Mater Chem B*. 2017;25:4863–4875. doi:10.1039/C7TB00833C
43. Zhang Y, Xiu W, Sun Y, et al. RGD-QD-MoS2 nanosheets for targeted fluorescent imaging and photothermal therapy of cancer. *Nanoscale*. 2017;41:15835–15845. doi:10.1039/C7NR05278B
44. Cui L, Xiong C, Zhou M, Shi S, Chow DS, Li C. Integrin αvβ3-targeted [64 Cu]CuS nanoparticles for PET/CT imaging and photothermal ablation therapy. *Bioconjugate Chem*. 2018;29:4062–4071. doi:10.1021/acs.bioconjchem.8b00690
45. Mao B, Liu C, Zheng W, et al. Cyclic cRGDfk peptide and Chlorin e6 functionalized silk fibroin nanoparticles for targeted drug delivery and photodynamic therapy. *Biomaterials*. 2018;45:306–320. doi:10.1016/j.biomaterials.2018.01.045
46. Bao H, Zhang H, Zhou L, et al. Ultrathin and isotropic metal sulfide wrapping on plasmonic metal nanoparticles for surface enhanced ram scattering-based detection of trace heavy-metal ions. *ACS Appl Mater Inter*. 2019;11:28145–28153. doi:10.1021/acsami.9b05878
47. Xu X, Sabanayagam CR, Harrington DA, Farach-Carson MC, Jia X. A hydrogel-based tumor model for the evaluation of nanoparticle-based cancer therapeutics. *Biomaterials*. 2014;35:3319–3330. doi:10.1016/j.biomaterials.2013.12.080
48. Becue A, Scoundrianos A, Moret S. Detection of fingermarks by colloidal gold (MMD/SMD) – beyond the pH 3 limit. *Forensic Sci Int*. 2012;219:39–49. doi:10.1016/j.forsciint.2011.11.024
49. Ali MR, Wu Y, Han T, et al. Simultaneous time-dependent surface-enhanced raman spectroscopy, metabolomics, and proteomics reveal cancer cell death mechanisms associated with gold nanorod photothermal therapy. *J Am Chem Soc*. 2016;138:15434–15442. doi:10.1021/jacs.6b08787
50. Zhang F. Physicochemical properties and mechanisms of drug release from melt-extruded granules consisting of chlorpheniramine maleate and Eudragit FS. *Drug Dev Ind Pharm*. 2016;42:563–571. doi:10.3109/03639045.2015.1054832
51. Faridli Z, Mahani M, Torkzadeh-Mahani M, Fasihi J. Development of a localized surface plasmon resonance-based gold nanobiosensor for the determination of prolactin hormone in human serum. *Anal Biochem*. 2016;495:32–36. doi:10.1016/j.ab.2015.11.016
52. Feng N, Liu Y, He M, et al. Delivery of vincristine sulfate-conjugated gold nanoparticles using liposomes: a light-responsive nanocarrier with enhanced antitumor efficiency. *Int J Nanomed*. 2015;10:3081. doi:10.2147/IJN.S79550
53. Kheirkhah P, Denyer S, Bhimani AD, et al. Magnetic drug targeting: a novel treatment for intramedullary spinal cord tumors. *Sci Rep*. 2018;8:1–9.
54. Browning RJ, Reardon PJT, Parhizkar M, et al. Drug delivery strategies for platinum-based chemotherapy. *ACS Nano*. 2017;11:8560–8578. doi:10.1021/acsnano.7b04092
55. Favi PM, Valencia MM, Elliott PR, et al. Shape and surface chemistry effects on the cytotoxicity and cellular uptake of metallic nanorods and nanospheres. *J Biomed Mat Res A*. 2015;103:3940–3955. doi:10.1002/jbm.a.35518
56. Mohebbi S, Tohidi Moghadam T, Nikkhah M, Behmanesh M. RGD-HK peptide-functionalized gold nanorods emerge as targeted biocompatible nanocarriers for biomedical applications. *Nanoscale Res Lett*. 2019;14:13. doi:10.1186/s11671-018-2828-3
57. Sun Y, Liang Y, Dai W. Peptide-drug conjugate based nanocombination actualizes breast cancer treatment by maytansinoid/photothermia with assistance of fluorescent/photoacoustic images. *Nano Lett*. 2019;19(5):3229–3237. doi:10.1021/acs.nanolett.9b00770
58. Lu W, Melancon MP, Xiong C, et al. Effects of photoacoustic imaging and photothermal ablation therapy mediated by targeted hollow gold nanospheres in an orthotopic mouse xenograft model of glioma. *Cancer Res*. 2011;71:6116–6121. doi:10.1158/0008-5472.CAN-10-4557
59. Zhao Y, Liu W, Tian Y, et al. Anti-EGFR peptide-conjugated triangular gold nanoplates for computed tomography/photoacoustic imaging-guided photothermal therapy of non-small cell lung cancer. *ACS Appl Mater Interfaces*. 2018;10:16992–17003. doi:10.1021/acsami.7b19013
60. Wang X, Lv F, Li T, et al. Electrospun micropatterned nanocomposites incorporated with Cu2 S nanoflowers for skin tumor therapy and wound healing. *ACS Nano*. 2017;11:11337–11349. doi:10.1021/acsnano.7b05858
61. Gautam M, Poudel K, Yong CS, Kim JO. Prussian blue nanoparticles: synthesis, surface modification, and application in cancer treatment. *Int J Pharm*. 2018;549:31–49. doi:10.1016/j.ijpharm.2018.07.055